Article

Spatiotemporal Evolution and Impact Mechanisms of Areca Palm Plantations in China (1987–2022)

Cai Wang [1,2], **Zhaode Yin** [1,2], **Ruoyu Luo** [2], **Jun Qian** [1,3], **Chang Fu** [4], **Yuling Wang** [1], **Yu Xie** [2], **Zijia Liu** [1], **Zixuan Qiu** [1,2,3,*] **and Huiqing Pei** [5,*]

1   School of Breeding and Multiplication (Sanya Institute of Breeding and Multiplication), Hainan University, Sanya 572025, China; caiwang018@hainanu.edu.cn (C.W.); zhaodeyin@hainanu.edu.cn (Z.Y.); yjsxjgl@hainanu.edu.cn (J.Q.); yulingw@hainanu.edu.cn (Y.W.); liuzijia@hainanu.edu.cn (Z.L.)
2   Intelligent Forestry Key Laboratory of Haikou City, School of Tropical Agriculture and Forestry, Hainan University, Haikou 570228, China; ruoyuluo@hainanu.edu.cn (R.L.); xieyu@hainanu.edu.cn (Y.X.)
3   School of Information and Communication Engineering, Hainan University, Haikou 570228, China
4   School of Design, Hainan Vocational University of Science and Technology, Haikou 571125, China; fuchang@hainanu.edu.cn
5   Department of Global Agricultural Sciences, Graduate School of Agricultural and Life Sciences, The University of Tokyo, Tokyo 113-8657, Japan
*   Correspondence: zixuanqiu@hainanu.edu.cn (Z.Q.); peihq@g.ecc.u-tokyo.ac.jp (H.P.); Tel.: +86-15600804604 (Z.Q.)

Abstract: This study delved into the spatiotemporal evolution and impact mechanisms of areca palm (*Areca catechu* L.) plantations in China. Using Landsat and Google Earth imagery combined with machine learning, the geographical distribution of areca palm was mapped at a 30 m resolution from 1987 to 2022, achieving an overall classification accuracy of 0.67 in 2022. The plantation area rapidly expanded from 8064 hectares in 1987 to 193,328 hectares in 2022. Spatially, there was a pronounced trend of overall agglomeration in areca palm plantations, primarily displaying two distribution patterns: high-value aggregation and low-value aggregation. Moreover, the plantation area exhibited a significant positive correlation with both GDP (r = 0.98, $p < 0.001$) and total population (r = 0.92, $p < 0.01$), while negatively correlating with rural population (r = −0.76, $p < 0.05$). No significant correlation was observed with environmental factors. This study elucidated the patterns and trends concerning economic development across regions and the impact of monoculture on Hainan Island's ecological environment. Comprehensive, large-scale, long-term mapping of areca palms will enhance our understanding of global agriculture's sustainability challenges and inform policy development.

Keywords: areca palm; spatiotemporal evolution; influential mechanism; sustainability

1. Introduction

In recent years, the global area dedicated to cash crop cultivation has been steadily increasing [1]. This has resulted in economic benefits for the regions cultivating these crops and acceleration of regional and global trade interactions [2]. However, the expansion of cash crops creates complex issues that require in-depth analysis from multiple perspectives to ensure sustainability [3–5]. In some areas, specific cash crops have become an integral part of the daily lives of the local people and subsequently shaped their spiritual attributes and social values [6–8]. However, this has seriously harmed natural ecosystems, such as tropical rainforests. For example, the expansion of *Hevea brasiliensis* rubber plantations and oil palm was a key driving factor behind deforestation, carbon emissions, and biodiversity loss in Southeast Asia. Furthermore, in Southeast Asia, the overcultivation of some cash crops is threatening the ecological balance and biodiversity of nature reserves [9,10]. Areca palm (*Areca catechu* L.) is an important cash crop grown in the tropics of India and Southeast Asia [11]. In China, areca palm is mainly distributed in tropical areas such as Yunnan, Hainan, and Taiwan [12] but is primarily cultivated in the Hainan province, where the

cultivation area, annual production, and procurement volume account for over 99% of the Chinese total [13], and it is mainly processed in Hainan Province. Betel nuts contain arecoline and arecaidine, which can stimulate the secretion of endogenous adrenocortical hormones and adrenaline, resulting in an increased level of adrenocortical hormones and energizing effects; however, they can be addictive [14]. In recent decades, the consumption of betel nuts and the incidence of oral cancer have sharply increased in the Asia-Pacific region [15–18], and a considerable proportion of the population also engages in betel nut chewing [19]. Local social and cultural factors also contribute to the prevalence of betel nut chewing [20], and consequently, the economic value of areca palm has markedly increased [21], and in China, it is close to 100 billion yuan each year. Since 1998, Hainan betel nuts have been sold directly after ripe picking or simple preliminary processing and then resold to enterprises in Hunan and Guangxi for further processing. Therefore, it is necessary to explore the mechanisms of areca palm impact.

Betel nuts were initially introduced as a food product in Xiangtan, Hunan, and the industry has since taken root in many other regions, including Hubei, Jiangxi, Guizhou, Guangdong, and Heilongjiang, and this has been driven by market demand, capital investment, and advertising. However, owing to a series of social, health, and environmental issues associated with areca palm, on 7 March 2019, the Hunan Betel Nut Advertising called for all betel nut enterprises in Hunan Province to cease any form of product advertising within the province [22]. Areca palm has since become the focus of international attention, and there is an urgent need for an in-depth understanding of the spatial distribution of areca palm plantation, as well as an analysis of its responses and adaptive mechanisms to local social, economic, and climatic factors to facilitate sustainable regional development decision-making and future-related analyses. At present, large-scale and long-term distribution data for areca palm are not available.

Crop spatial distribution mapping research uses optical and radar satellites, including Landsat, Sentinel-2, MODIS, SPOT, QuickBird, Sentienl-1, Worldview, GeoEye-1, and ALOS PALSAR [23–25]. In general, remote sensing data must be combined with corresponding classification algorithms for accurate crop spatial distribution mapping. For instance, **Freudenberg et al.** proposed a neural network of the U-Net to detect oil and coconut palms on high-resolution satellite images with accuracies between 89% and 92% [26]. **Li** used a number of manually interpreted samples to train and optimize the convolutional neural network (CNN) and detected 96% of the oil palm trees using the QuickBird images compared with the manually interpreted ground truth [27]. **Cheng** combined PALSAR-2 with a maximum likelihood classifier (MlC) to map the oil palm with a 1 km meter resolution in Malaysia, which is the closest to the official MPOB inventories (~8.87% overestimation) [28]. Lee tested two classification algorithms Classification and Regression Trees (CART) and Random Forests (RF) and evaluated various band combinations for extracting oil palm in India using Landsat 8 imagery [29]. Li matched crop classifications using the Random Forest algorithm with area estimations based on samples and generated 10 m resolution maps for maize and soybean in China using sentinel-2 data [30]. **Johnson** utilized historical Landsat data to create historical crop maps for the United States [31], and **Carrasco** employed historical Landsat data to produce distribution maps for the rice fields in Japan [32]. In these previous cases, medium- to low-resolution remote sensing data were used to map crops at a large scale. When mapping the large-scale and long-term crops, Landsat remote sensing data are indispensable [33].

This has previously been challenging, as many of the crop plantations are cultivated by individual farmers, resulting in a scattered planting pattern [34]. Landsat data generally have poorer recognition ability for crops with scattered planting patterns due to its resolution limitations [35]. However, if the potential range and geographic distribution information of the crops can be obtained, it is still possible to achieve good classification results by leveraging this prior knowledge. This is because known prior knowledge, such as slope, distribution area, and potential range of distribution, can help guide and refine the classification algorithm to more accurately identify target areas, compensating for

the limitations of the satellite data resolution [36]. The potential range limitation of the distribution of classification results is an effective method of spatial constraint. In other crop mapping, one category of existing land classification data is often used as the potential distribution range of the crop. However, the actual planting situation of areca palm is very complicated, and the existing land classification data do not meet the requirements of its potential distribution range. In a preliminary study mapping mangroves, **Jia** determined their potential range by expanding the extent of existence [37]. To reconstruct global wetland loss, **Fluet-Chouinard** used currently available wetland extents to generate a potential wetland distribution range [38]. The potential distribution range is constructed on the basis of the original data, so the existing areca palm distribution information must be obtained.

High-resolution imagery is necessary for precise areca palm potential distribution mapping, as when compared to low-resolution imagery, it can provide richer feature information. Consequently, however, feature selection and robust model-processing capabilities are required to process this data [39,40]. Deep learning can extract features layer-by-layer from raw data [41,42] and is more suitable for big data than traditional machine-learning models [43,44]. Google Earth was released in 2005 and enabled users to download high-resolution images, which have since been utilized by hundreds of millions of users worldview, and this has had a profound impact on both academia and industry [45]. Google satellite imagery is not a single data source but an integration of satellite and aerial photography. Some of its satellite imagery was sourced from WorldView-2, WorldView-3, and QuickBird-2, all of which belong to the Digital Globe (Westminster, CO, USA).

This study has aimed to collaboratively map the spatial distribution of the areca palm in the Hainan region of China across a large-scale and long-term with high- and medium-resolution imagery, as well as machine-learning and deep-learning techniques, and has also investigated the spatiotemporal dynamics of the areca palm and the influencing mechanisms (Figure 1). The main research objectives were as follows: (1) map the potential range of the areca palm; (2) dynamic change and spatial pattern of the areca palm; and (3) mechanisms influencing area palm evolution. This study will help to address the challenges of agricultural sustainability globally and serve as a reference for related policies.
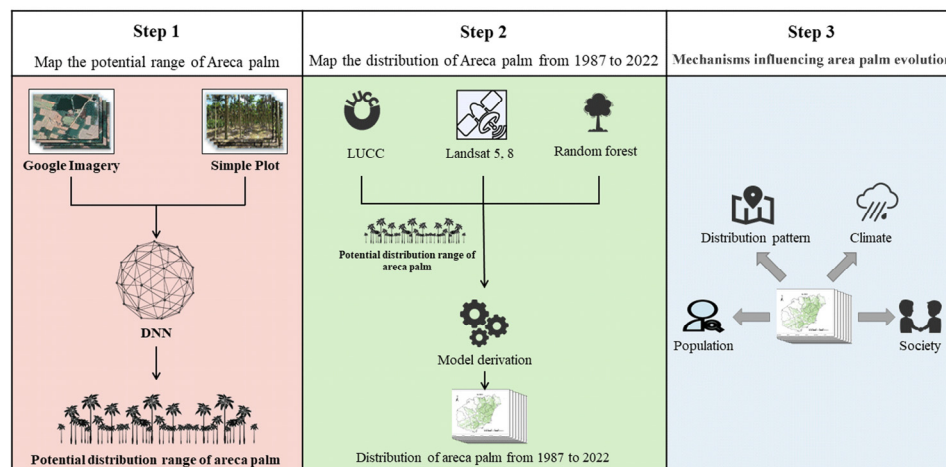
Figure 1. Overall research flow chart.

2. Materials and Methods

2.1. Materials

2.1.1. Study Area

Hainan Island is located between 108°21′ and 111°03′ east longitude and 19°20′ to 20°10′ north latitude. It covers 33,900 km², making it the largest and southernmost island in the People's Republic of China. It has an oceanic tropical monsoon climate, situated on the northern edge of the tropics, with long summers and no winters. The annual average temperature is 22–26 °C and the cumulative temperature above 10 °C reaches

8200 °C. Even in the coldest months of January and February, the temperature range is 16–21 °C. The annual sunshine duration range is 1750–2650 h, with sunshine ratios of 50% to 60%. Abundant sunlight and favorable temperatures increase the photosynthetic potential, making the area suitable for areca palm cultivation. In fact, Hainan Island is the primary production area of areca palms in China, as it accounts for 99% of the total national production. Areca palm cultivation is widespread across 18 counties and cities in Hainan. The overall view of the study area is shown in Figure 2, and the complete name, short form, and abbreviation for each of these areas are given in Table 1.
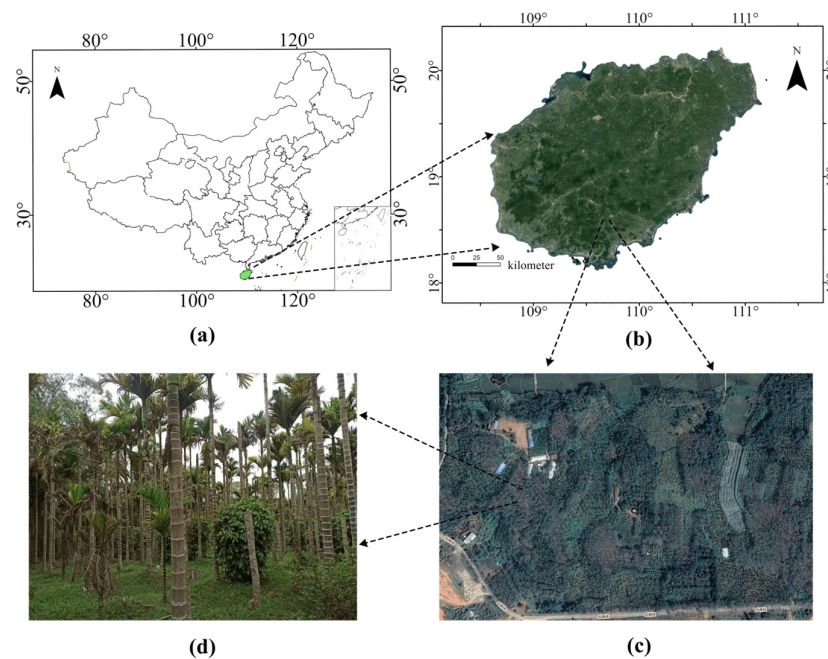

Figure 2. Overall view of the study area: (**a**) administrative map of China, (**b**) remote sensing images of Hainan, (**c**) areca palm (*Areca catechu* L.) on Google images, and (**d**) mobile phone photograph of areca palm.

Table 1. The complete name, short form, and abbreviation for each county and city in Hainan.

Complete Name	Short Form	Abbreviation
Baisha Li Autonomous County	Baisha	BS
Baoting Li and Miao Autonomous County	Baoting	BT
Changjiang Li Autonomous County	Changjiang	CJ
Chengmai County	Chengmai	CM
Danzhou City	Danzhou	DZ
Ding'an County	Ding'an	DA
Dongfang City	Dongfang	DF
Haikou City	Haikou	HK
Ledong Li Autonomous County	Ledong	LD
Lingshui Li Autonomous County	Lingshui	LS
Lingao County	Lingao	LG
Qionghai City	Qionghai	QH
Qiongzhong Li Autonomous County	Qiongzhong	QZ
Sanya City	Sanya	SY
Tunchang County	Tunchang	TC
Wanning City	Wanning	WN
Wenchang City	Wenchang	WC
Wuzhishan City	Wuzhishan	WZS

2.1.2. Image Data Sources

Digital orthophotos were sourced from QuickBird-2, Geoeye-1, WorldView-2, and WorldView-3, which contain only RGB three-channel information. They were downloaded from the Google Historical Imagery server, with a resolution of 0.59 m, and ranging from November 2021 to February 2023. For the selection of digital orthophotos, images with minimal cloud cover, consistent overall color tones, and clear imaging were selected. For ease of data storage, they were cropped into 256×256-pixel tiles, and there was a total of 2,610,000 tiles.

Landsat Surface Reflectance (SR) data, with a spatial resolution of 30 m, were downloaded from the Google Earth Engine (GEE) platform. The Landsat 5 SR products have been processed using the Landsat ecosystem disturbance adaptive processing system (LEDAPS) [46] on the GEE platform. The steps included geometric correction, radiometric correction, atmospheric correction, and topographic correction. The Landsat 8 SR products are created with the Land Surface Reflectance Code (LaSRC) [47]. The image selection criteria included cloud cover of less than 20% and high imaging quality. Cloud removal was performed using the QA-PIXEL band. To ensure consistency in the extraction of bands across each of the years for which the Landsat acquisition data were obtained, six common bands were shared by the Landsat satellite, namely, blue, green, near-infrared (NIR), short-wave infrared 1 (SWIR1), and short-wave infrared 2 (SWIR2), and they were extracted and composited using an annual median synthesis method. The study area encompasses a large area, and in practical operations, the results of the annual compositing often suffer from data gaps due to cloud cover. To address this problem, a data supplementation approach was adopted by selecting images from adjacent years with low cloud cover for the median composition. This ultimately helped to reduce data loss. The information on image composition time, satellite sensor, and selected bands used in this study is given in Table 2.

Table 2. Landsat data images and information used in the study.

Year	Image Composition Time	Satellite Sensor	Bands Information
1987	01/01/1987–30/12/1987		Blue (0.45–0.52 μm)
1992	01/01/1992–01/03/1993		Green (0.52–0.60 μm)
1997	01/01/1997–30/12/1997		Red (0.63–0.69 μm)
2002	01/10/2001–30/12/2002	Landsat5 TM	NIR (0.77–0.90 μm)
2007	01/01/2007–30/12/2007		SWIR1 (1.55–1.75 μm)
2012	01/06/2011–01/05/2012		SWIR2 (2.08–2.35 μm)
			Blue (0.452–0.512 μm)
2017	01/01/2017–30/12/2017		Green (0.533–0.590 μm)
			Red (0.636–0.673 μm)
		Landsat8 OLI	NIR (0.851–0.879 μm)
2022	01/01/2022–30/12/2022		SWIR1 (1.566–1.651 μm)
			SWIR2 (2.107–2.294 μm)

2.1.3. Ground Survey Data Sources

From March 2023 to August 2023, our team conducted surveys at the areca palm plantations in each county and city within Hainan Province. Each number used a handheld GPS (Garmin GPSMAP 63csx) in conjunction with Google Earth (Google Inc., Santa Clara County, CA, USA) to record and store data detailing the distribution of the areca palm samples. To ensure spatial representativeness, we maintained a distance of approximately 1 km between two areca palm samples. Ultimately, data for 1500 areca palm sample plots are shown in Table 3. Our research divided the areca nut survey plots into three equal parts in order to analyze and construct a more reasonable areca palm classification model. The first set of 500 areca palm sample plots was used for training the deep learning model, with the data split into 70% for training and 30% for validation. The second set of 500 areca palm sample plots was reserved exclusively for testing the model's classification performance. The third set comprised 500 areca palm sample plots and 500 other land cover sample plots,

which were used to evaluate the practical accuracy of the Random Forest model that was developed. The distribution of different areca palm sample plots is shown in Figure 3.

Table 3. The survey information of the areca palm plot.

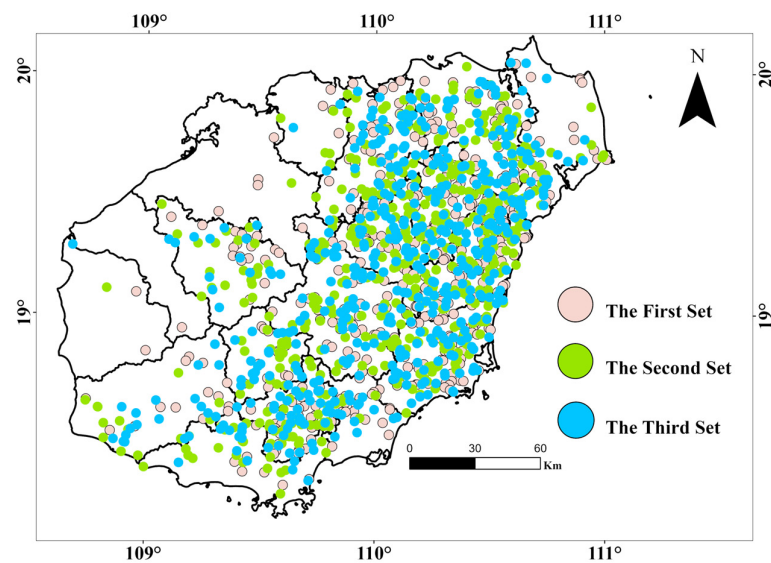| Cities/Counties	Areca Palm Plot	Average Area (ha)
BS	56	0.98
BT	105	2.65
CJ	1	0.86
CM	122	2.78
DZ	5	1.71
DA	136	3.42
DF	4	1.35
HK	132	1.57
LD	44	1.88
LS	13	3.61
LG	44	2.22
QH	211	4.78
QZ	154	2.44
SY	44	1.38
TC	114	3.78
WN	167	2.65
WC	97	1.21
WZS	51	2.11

Figure 3. Areca palm sample plots distribution in Hainan Province.

2.1.4. Auxiliary Data Sources

Historical climate data were downloaded from the WorldClim website (https://www.worldclim.org) accessed on 5 April 2023. This website provides historical monthly data from 1960 to 2021, downscaled from the CRU-TS-4.0.6 data by the Climatic Research Unit at the University of East Angelia. The available variables include average minimum temperature (°C), average maximum temperature (°C), and total precipitation (mm). These data are provided at three spatial resolutions: 2.5 min (approximately -21 km^2 at the equator), 5 min (approximately -85 km^2 at the equator), and 10 min (approximately -340 km^2 at the equator). Three variables were selected at a spatial resolution of 2.5 min. Data processing, including annual compositing and cropping, was conducted using Python 3.10 with packages such as numpy, os, rasterio, and geopandas. This resulted in the generation of annual historical weather data for the study area. The total population, urban population, rural population, and GDP were sourced from the 1988, 1993, 1998,

2003, 2008, 2013, 2018, and 2022 Hainan Statistical Yearbooks, which typically release statistical data beginning in December of the previous year. To ensure data consistency, this study uses climate and statistical data from 2021 to represent the climate and economic conditions of Hainan Island in 2022. Furthermore, the 2022 land use data used in this study were sourced from Dynamic World V1, a 10 m near-real-time (NRT) Land Use Land Cover (LULC) dataset created by Dynamic World [48]. This dataset includes class probabilities and label information for the nine classes. The classification system comprises nine categories: water, trees, grass, flooded, vegetation, crops, shrubs, built, bare, snow, and ice. These data are available for download on the GEE platform. In this study, 2022 land use data points for Hainan Island were generated on the GEE platform using the annual maximum value composite method.

2.2. Methods

2.2.1. Mapping the Areca Distribution with Deep Learning

Compared to the data obtained from medium- and high-resolution images, the data obtained from high-resolution images are richer and of a greater data magnitude. However, high-resolution images require greater computational power to process. Convolutional neural networks (CNNs) provide an effective approach for automatically extracting features from raw images using a mathematical operation known as convolution, making them suitable for processing large datasets. In this study, ResNet 50 was employed as the backbone model. During the training of deep neural networks, issues such as vanishing and exploding gradients often occur. ResNet addresses these challenges by introducing residual modules that allow the network to skip certain layers, thereby enabling it to learn identity mappings and effectively train deep networks [49]. The "50" in ResNet 50 represents the depth of the network and, thus, the total number of layers, including the convolutional, pooling, and fully connected layers. Depth is generally considered a crucial factor for improving neural network performance, where deeper networks theoretically offer stronger learning capabilities but generally require more memory. Given these considerations, ResNet50 was chosen due to its balance between performance and memory usage. In this study, a specific structure called the three-level ResNet unit was utilized, as illustrated in Figure 4. The basic architecture of the model was inspired by U-Net, which was originally introduced by **Romeberger** for image segmentation in medical imaging [50] and has since been repeatedly shown to be an effective tool for the classification of remote sensing images [51–54]. U-Net's name comes from its shape, as its network structure resembles the letter "U", as it consists of both encoding and decoding paths. In the encoding path, the feature maps are gradually reduced in scale while increasing the number of channels, similar to a typical convolutional neural network. In the decoding path, an upsampling operation (deconvolution or interpolation) is used to progressively restore the scale of feature maps. The feature maps at the corresponding levels in the encoding path are directly connected to those in the decoding path, allowing for the transmission of multi-scale feature information. The connection is referred to as a skip connection and aids in recovering local details and providing contextual information. In the final layer of the decoding, a softmax activation function is applied to convert the raw scores at each pixel into values representing the probabilities of different classes by completing the segmentation. U-Net model surpasses conventional image classification methods in accurately segmenting different crop types [54] Combining ResNet 50 with U-net to form Res50_U-net enhances performance, leveraging the strengths of both architectures to ensure areca palm classification results. The structure of the Res50_U-net model is illustrated in Figure 5.
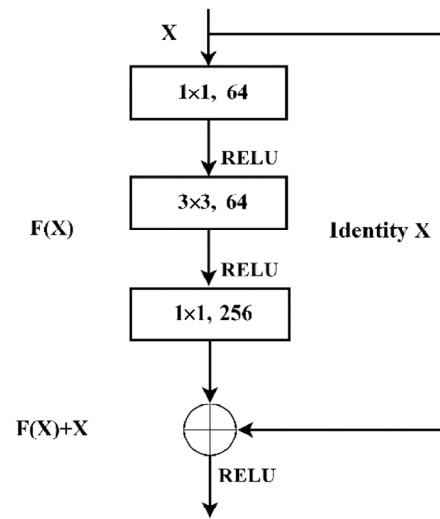
Figure 4. Network structure of residual learning. "F(x)" refers to the residual and "x" is the feature mapping of the output of the previous layer ResNet.
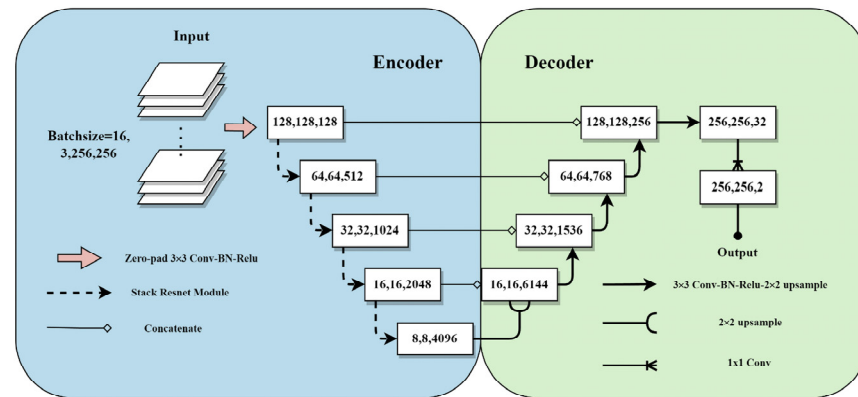

Figure 5. Network structure of Res50_U-net.

During the model training process, cross-entropy loss was employed as the optimization objective to guide the training, as shown in Equation (1).

$$Loss = -\frac{1}{n} 1ny_i \, log \, p_i + (1 - y_i) \, log \, (1 - p_i) \tag{1}$$

where n represents the batch size and y_i and p_i represent the truth and prediction values of the "i-th" sample in the current batch, respectively. Additionally, to ensure that the model can achieve a global optimal solution and avoid becoming stuck in local optima, this study employs the Adam optimizer, which is an adaptive optimization algorithm that helps the model converge to the optimal solution more quickly during training [55]. The parameter-updated formula is shown in Equation (2).

$$\theta_t \leftarrow \theta_{t-1} - \gamma \hat{m}_t / \left(\sqrt{\hat{v}_t} + \epsilon \right) \tag{2}$$

where t is the current training step, θ_t is the parameter at step t, θ_{t-1} is the parameter at step $t-1$, $\hat{m}_t$ is the biased-corrected first-order moment estimate, $\hat{v}_t$ is the biased-corrected second-order moment estimate, and ϵ is a constant used to prevent division by zero.

2.2.2. Multi-Data Fusion Combined with Machine Learning to Map Historical Areca Palm Distribution

Areca palm plantation is characterized by small patches and decentralization, making classification challenging. Although the distribution of areca palm can be accurately extracted using high-resolution images, it is currently difficult to obtain large-scale, long-term, and full-coverage high-resolution images. Given the long duration of the study, Landsat satellite data are the most suitable option since it provides the necessary coverage. Compared to high-resolution satellites, Landsat has a lower spatial resolution, which, when combined directly with ground survey data and classification algorithms, is likely to result in significant bias. Knowing the potential distribution range of the areca palm, however, can help to reduce bias. Therefore, in this study, the potential range of historical areca palm distributions was defined using the classification results from deep learning (as described in Section 2.2.1). The spatial distribution predictions were limited to this potential range. To account for the scale difference between the two resolutions, a 1 km buffer was added on both sides of this range to minimize the impact of the scale differences. For classifier selection, this study adopted a Random Forest model, which was constructed based on multiple decision trees and can reduce overfitting by introducing randomness into the dataset [56]. Another issue is that although we know the distribution of areca palms in 2022, we do not have information about the distribution of other land cover types. Therefore, in this study, 9-class cover data types from Dynamic World were used, (as described in Section 2.1.4), along with high-resolution areca palm data, resulting in the use of 10 data classes when building the training dataset. A Random Forest classification model was trained with 500 randomly selected training samples for each land-cover class. After training, the model was used in conjunction with Landsat data to infer the areca palm distribution in Hainan Island for 1987, 1992, 1997, 2002, 2007, 2012, 2017, and 2022. The model configuration, as shown in Figure 6, includes 200 decision trees and a maximum depth of 50. The choice of 200 decision trees was made to achieve a high level of accuracy and stability in the Random Forest model. This number balances performance with computational efficiency, as additional trees beyond 200 offered diminishing returns. The maximum depth of 50 was selected to capture complex relationships in the data while minimizing the risk of overfitting. This depth allows each tree to model intricate patterns without becoming excessively complex.
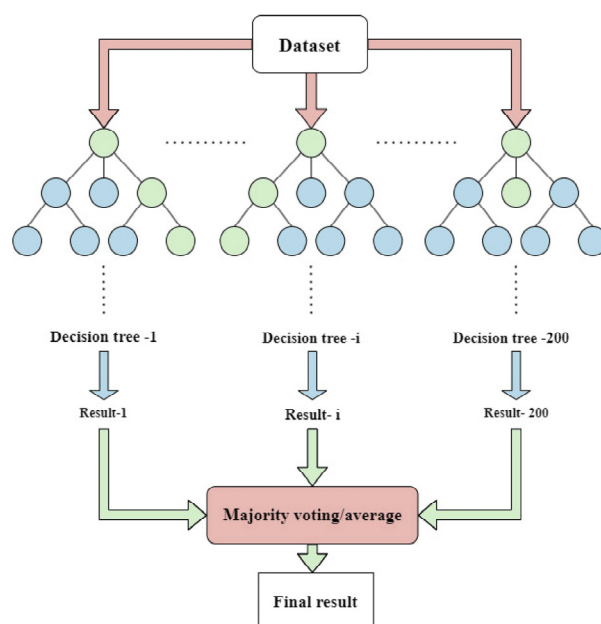

Figure 6. Network structure of Random Forest model used in the study.

2.2.3. Evaluation of the Classification Results

This study evaluated the deep learning classification results for the areca palm in 2022 based on two primary criteria. One of these criteria, referred to as internal model validation, involves dividing the dataset and using 70% for training and 30% for validation. The performance of the model when using the validation set was then assessed using classification metrics, including Dice and Precision and Recall, as shown in Equations (3)–(5). Dice measures the overlap between correctly classified positive class samples and actual positive class samples. Precision quantifies the proportion of true-positive samples among the samples predicted as positive by the model. Recall calculates the proportion of true-positive samples detected by the model from all actual positive class samples. A detailed explanation of the parameters for these three metrics is presented in Table 3.

$$Dice = \frac{2 \times TP}{TP + FP + TP + FN} \tag{3}$$

$$Precision = \frac{TP}{TP + FP} \tag{4}$$

$$Recall = \frac{TP}{TP + FN} \tag{5}$$

This study also includes an external model validation, which assesses the model's performance when classifying actual land cover types. In this part of the evaluation, a confusion matrix (Table 4) is constructed to calculate various classification metrics. These metrics include the User's Accuracy, Producer's Accuracy, and Overall Accuracy shown in Equation (6), F1 score in Equation (7), and the Kappa coefficient in Equation (8). The User's Accuracy and Producer's Accuracy are equivalent to those shown in Equations (5) and (4), respectively (Table 5).

$$OA = \frac{a + d}{a + b + c + d} \tag{6}$$

$$F1\text{-}score = 2\frac{Precision * Recall}{Precision + Recall} \tag{7}$$

$$kappa = \frac{OA - \frac{(a+b) \times (a+c) + (c+d) \times (b+d)}{(a+b+c+d)^2}}{1 - OA} \tag{8}$$

Table 4. Parameter explanation.

Parameter	Representation Results
TP	True positive (predicted as positive and actually positive)
FP	False positive (predicted as positive but actually negative)
TN	True negative (predicated as negative and actually negative)
FN	False negative (predicated as negative but actually positive)

Table 5. Confusion matrix.

Confusion Matrix		Reference Data		
		Areca	Non-Areca	Total
Classified data	Areca	a	b	$a + b$
	Non-Areca	c	d	$c + d$
	Total	$a + c$	$b + d$	$a + b + c + d$

An evaluation of the historical areca palm distribution dataset was also required. For large-scale, long-term land cover classification, permanent sample plot survey data are often lacking, especially for cash crops like the areca palm, as growers are often unwilling to

allow permanent sample plots in their plantations. Furthermore, it is difficult to guarantee the uniformity of cultivation in such plots. In this research, the areca palm range obtained from high-resolution imagery in 2022, with an added 1 km buffer, was used as the potential distribution. To validate the classification results based on the Random Forest, the third group of survey data was used as the reference data. The Confusion Matrix, Overall Accuracy (OA), and Kappa were computed to analyze the model's classification accuracy in 2022.

2.2.4. Dynamic Change and Spatial Pattern of Areca Analysis

The changes in the historical distributions of the areca palms in 1987, 1992, 1997, 2002, 2007, 2012, 2017, and 2022 were evaluated. Moreover, the historical spatial distribution patterns were explored using the classification results from these years. Since Hainan Island has 18 cities and counties that do not meet the minimum sample requirement of 30 for calculating the Global Moran's index, the analysis was conducted at the township level. First, the Global Moran's index was computed using Equation (9) to investigate the overall spatial correlation; then, based on the Global Moran's index, the Local Moran's index was calculated using Equation (10) to identify spatial clustering and dispersion phenomena [57]. The final spatial clustering results of the analysis include High-High-Cluster, High-Low-Cluster, Low-High-Cluster, Low-Low-Cluster, and Non-significant.

$$I = \frac{N}{W} \frac{\sum_{i=1}^{N} \sum_{j=1}^{N} \omega_{ij}(x_i - \overline{x})(x_j - \overline{x})}{\sum_{i=1}^{N} (x_i - \overline{x})^2} \tag{9}$$

where N is the number of spatial units indexed by i and j; x is the variable of interest; $\overline{x}$ is the mean of x; ω_{ij} are the elements of a matrix of spatial weights with zeros and diagonals (i.e., $\omega_{ij} = 0$); and W is the sum of all ω_{ij} (i.e., $W = \sum_{i=1}^{N} \sum_{j=1}^{N} \omega_{ij}$).

$$I_i = \frac{x_i - \overline{x}}{m_2} \sum_{j=1}^{N} \omega_{ij}(x_j - \overline{x}) \tag{10}$$

where $m_2 = \frac{\sum_{i=1}^{N} (x_i - \overline{x})^2}{N}$ then, $I = \sum_{i=1}^{N} \frac{I_i}{N}$, I is the Global Moran's index measuring global autocorrelation, I_i is local, and N is the number of analysis units on the map.

2.2.5. Statistical Analysis of Driving Forces

To investigate the influencing factors of climate and socioeconomics on cash crops, we discussed city- and county-scale data in relation to the areca palm distribution area from 1987 to 2022 and then explored the influencing factors that have played a major role in driving historical changes. These influencing factors were categorized into two groups: climatic factors, including total annual precipitation, maximum annual average temperature, and minimum annual average temperature; and socioeconomic factors, including gross domestic production, urban population, and rural population. To analyze the relationships among the time-series variables, we utilized the Pearson correlation coefficient shown in Equation (11) to describe the linear correlation between the areca palm area and other variables over the entire time range, thereby determining whether they exhibited synchronous changes.

$$\rho_{X,Y} = \frac{cov(X, Y)}{\sigma_X \sigma_Y} \tag{11}$$

where *cov* is the covariance, σ_X is the standard deviation of X, and σ_Y is the standard deviation of Y.

3. Results

3.1. Model Classifier Results

This study was conducted in a Windows 11 environment using Python 3.8.10 with a PyTorch deep-learning framework. The primary hardware includes an Intel i7 13700k CPU (16 cores, 24 threads, with a maximum turbo frequency of 5.40 GHz) and an NVIDIA GeForce RTK-4080 16 GB graphics card (NVIDIA, Santa Clara, CA, USA). Training samples were generated based on ground survey data and downloaded high-resolution imagery. These samples cover 18 counties and cities, including Baisha, Baoting, Changjiang, Chengmai, Danzhou, Dingan, Dongfang, Haikou, Ledong, Lingshui, Lingao, Qionghai, Qiongzhong, Sanya, Tunchang, Wanning Wenchang, and Wuzhishan, where there is areca palm plantation.

During the training of the Res50_U-net model, there were variations in the cross-entropy loss function (Figure 7). The loss function stabilized at 0.1 after 20,000 iterations. The training was then halted at this point, and the model parameters were recorded and saved.
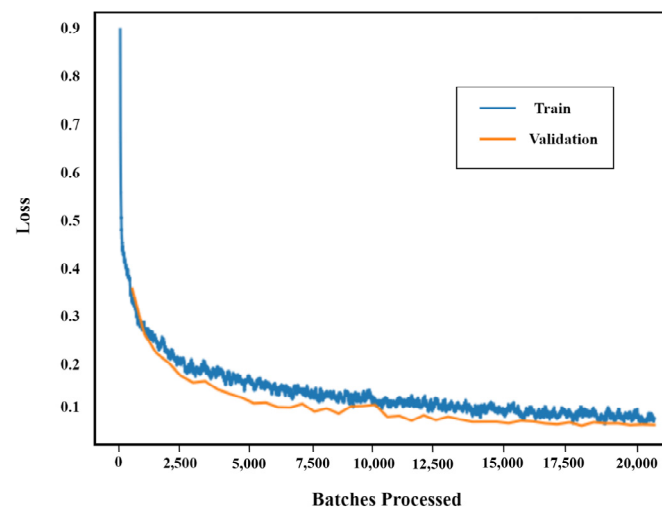

Figure 7. Res50_U-net cross-entropy loss curve, where the *x*-axis indicates the number of trainings' literation.

The classification performance of the validation set, which represents the internal evaluation of the model, is presented in Table 6. The precision value for "Non-Areca" is 0.98, the recall value is 0.97, and the Dice value is 0.97. This indicates that the model exhibits high consistency and accuracy in classifying "Non-Areca". While for "Areca", the precision value is 0.85, the recall value is 0.82, and the Dice value is 0.81. This suggests that the model demonstrates relatively high consistency and accuracy for the classification of "Areca", but there are some misclassifications. After reviewing the results of the internal model evaluation, external model validation was conducted. The model clearly performed well in the classification of the actual areca palm. The User's Accuracy and Producer's Accuracy for the areca palm are 0.87 and 0.92, respectively, indicating that the model performs well in the "Areca" category from both user and producer perspectives. The F1-Scores of 0.89 for areca palm and 0.90 for other land covers indicate that the model performs well in accurately distinguishing between them. Furthermore, the Overall Accuracy and Kappa coefficient suggest that the model exhibits outstanding performance in practical classification tasks with high accuracy and consistency in its predictions.

Table 6. Classification result of Res50_U-net.

Internal Evaluation	Areca	Non-Areca
Precision	0.85	0.98
Recall	0.82	0.97
Dice	0.81	0.97
External evaluation		
User's Accuracy	0.87	0.93
Producer's Accuracy	0.92	0.88
F1-Score	0.89	0.90
Overall Accuracy	0.90	
Kappa coefficient	0.80	

Furthermore, to provide readers with a more intuitive view of the actual classification results, a comparison between the Ground Truth and Res50_U-net classification results is provided for 18 counties and cities, including Baisha, Baoting, Changjiang, Chengmai, Danzhou, Dingan, Dongfan, Haikou, Ledong Lingshui, Lingao, Qionghai, Qiongzhong, Sanya, Tunchang, Wanning, Wenchang, and Wuzhishan, as shown in Figure 8.
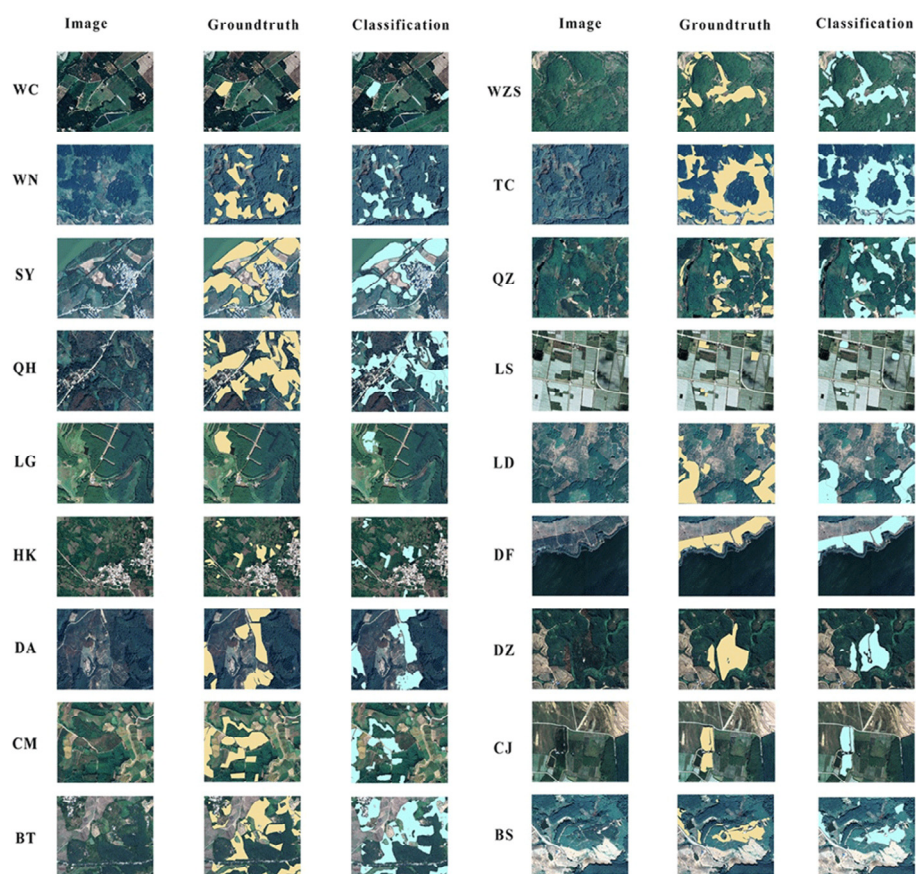

Figure 8. Illustrative examples of the classification method of Res50_U-net.

After completing the accuracy assessment for the areca palm distribution using deep learning, the classification results for the areca palms in 2022 were also calculated using the Random Forest model. The Overall Accuracy and Kappa coefficients are presented in Table 7. For the "Non-Areca", the user's classification accuracy is 0.66, and the producer's accuracy is 0.69. For the "Areca", the user's classification accuracy is 0.68, and the producer's accuracy is 0.65. The F1-Scores of 0.66 for areca palm and 0.67 for other land covers. The overall accuracy of the model is 0.67, and the Kappa coefficient is 0.34. The model has some ability to identify areca palms, but its performance is affected by the scale and

the fragmented, small-scale nature of their cultivation. Compared with the deep-learning classification results for the high-resolution imagery, the accuracy decreased. Overall, the model exhibits a certain degree of areca palm recognition capability.

Table 7. Classification result of Random Forest.

	User's Accuracy	Producer's Accuracy	F1-Score	Overall Accuracy	Kappa Coefficient
Areca	0.68	0.65	0.66	0.67	0.34
Non-Areca	0.66	0.69	0.67		

3.2. Dynamic Change and Spatial Pattern of Areca Palm

After validating the accuracy of the Random Forest model, it was used to deduce the historical distributions of the areca palm on Hainan Island by comparing the changes in coverage in 1987, 1992, 2002, 2007, 2012, 2017, and 2022 (Figures 9 and 10, and Table 8). From a holistic perspective, the areca palm area on the island increased significantly from 8.064 ha in 1987 to 193.308 ha in 2022, exhibiting exponential growth. Areca palm is distributed in all cities and counties on Hainan Island, and based on cultivation areas, it can be roughly categorized into three groups: (1) Changjiang, Danzhou, Dongfang, and Lingao, which have smaller areca palm cultivation areas (<2000 ha) with minimal growth; (2) Baisha, Ledong, Sanya, Wuzhishan, and Lingshui, which have areca palm cultivation areas ranging from 2000 to 10,000 ha, indicating large-scale cultivation with substantial growth; and (3) Baoting, Chengmai, Ding'an, Qionghai, Haikou, Wengchang, Wanning, Tunchang, and Qiongzhong, which have both large-scale areca palm plantation and significant growth in plantation areas.
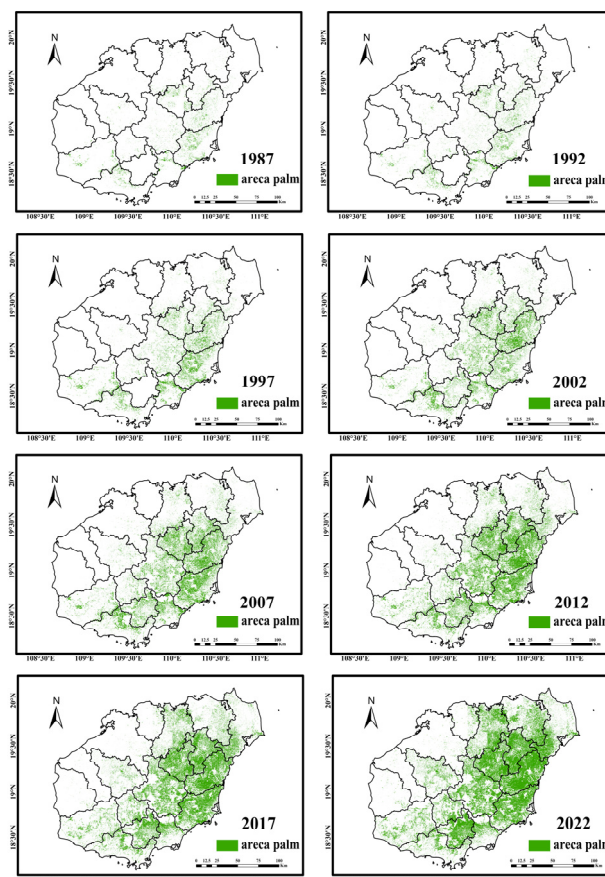

Figure 9. Distribution of areca palm plantation in the Hainan Island during 1987–2022.
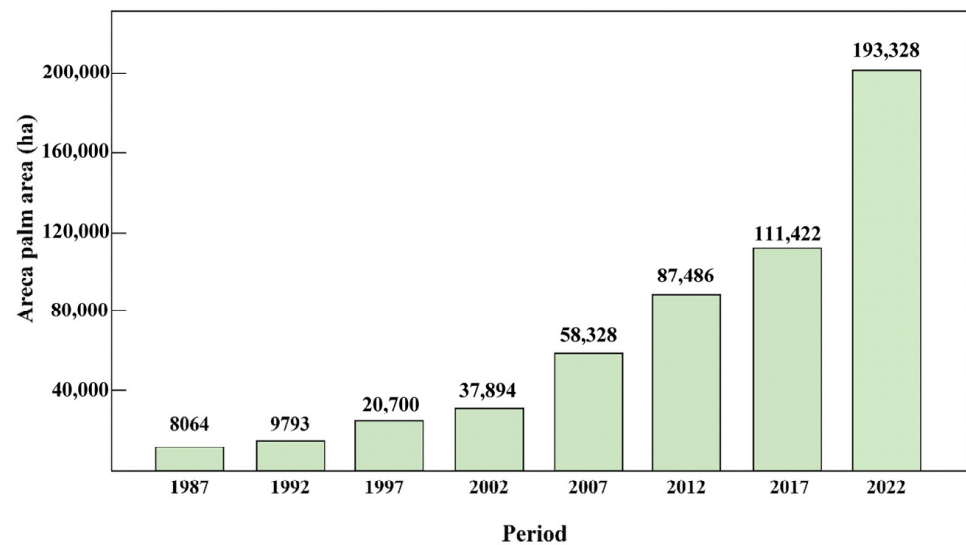
Figure 10. Trends of areca palm area in the Hainan Island during 1987–2022.

Table 8. Areca palm plantation area (ha) in the Hainan Island.

	Areca Palm Area (ha)							
	1987	**1992**	**1997**	**2002**	**2007**	**2012**	**2017**	**2022**
Baisha	176	221	93	343	539	537	1330	3787
Baiting	506	687	1092	1609	3277	4435	5961	14,449
Changjiang	0	0	0	0	0	19	51	121
Chengmai	144	142	386	1010	2069	3409	5308	14,390
Danzhou	11	11	13	35	297	118	330	574
Dingan	330	257	707	1380	4488	8327	10,792	19,192
Dongfang	26	26	2	6	6	36	123	379
Haikou	77	221	311	239	785	1636	2213	11,600
Lengdong	876	910	2423	1874	2724	3625	4272	6248
Linggao	0	0	0	1	6	68	404	1427
Lingshui	1155	1641	3786	3491	3942	4503	4395	4277
Qionghai	864	1012	3103	8537	8993	15,932	17,755	33,906
Qiongzhong	529	529	1799	5134	6086	12,500	14,934	22,484
Sanya	664	945	1463	3569	4763	4243	4742	4774
Tunchang	837	1013	1420	3878	6500	9601	11,922	19,390
Wangning	1698	1896	3469	6446	12,259	15,629	19,157	21,739
Wengchang	48	67	234	158	667	1585	4788	10,024
Wuzhishan	123	215	399	184	927	1283	2945	4567
Total	8064	9793	20,700	37,894	58,328	87,486	111,422	193,328

Figure 11 illustrates the Global Moran's Index for areca palms on Hainan Island from 1987 to 2022. The Global Moran's Index measures the degree to which similar values are clustered within the study area. Over the period, the index shows an increasing trend, peaking at 0.45 in 1997 and 0.51 in 2012, indicating a significant positive spatial correlation. This suggests that areca palms have become more spatially clustered over time. Figure 12 presents the Local Moran's Index, which provides insights into specific clustering and dispersion patterns within the island. This detailed spatial analysis helps to understand the distribution and changes in areca palm cultivation from 1987 to 2022.
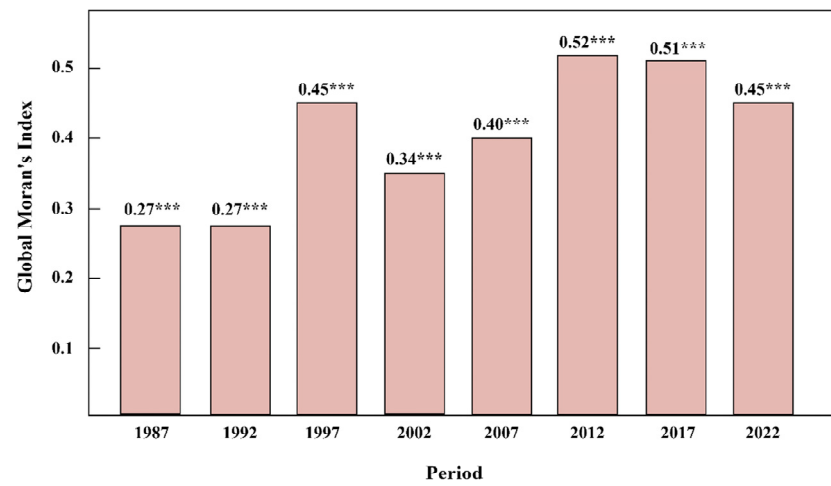
Figure 11. Trends of areca palm's Global Moran's Index in Hainan Island from 1987 to 2022 (*** $p < 0.001$).
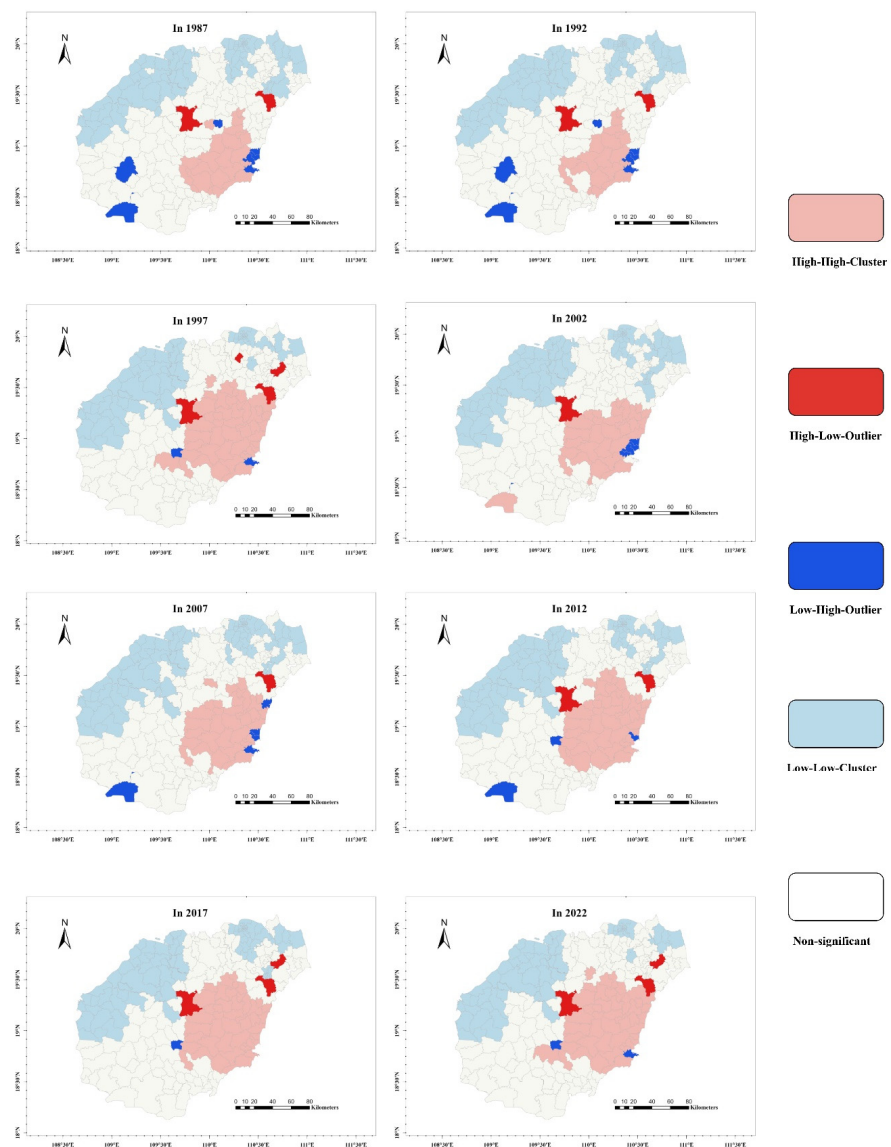

Figure 12. The Local Moran's Index of Hainan Island from 1987 to 2022.

3.3. Mechanisms Influencing Area Palm Evolution

The total population of Hainan Island showed a steady upward trend from 1987 to 2022, from 5.66 million in 1987 to 10.23 million in 2022. The rural population is stable, while the urban population increases steadily each year. Hainan Island's GDP shows an obvious upward trend from 1987 to 2022, growing rapidly from 24.6 billion yuan in 1987 to 6818 billion yuan in 2022 (Figure 13). At the same time, temperature changes on Hainan Island are relatively stable, while the precipitation showed fluctuating annual precipitation, with increases from 1109 mm in 1987 to peaks like 1917 mm in 2012, followed by decreases, reaching 1590 mm in 2022 (Table 9).
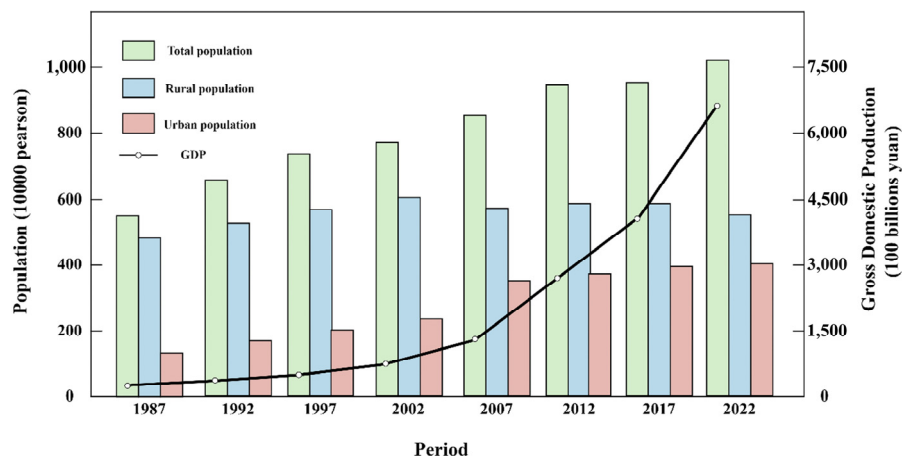

Figure 13. Climate and environmental indicator dynamics in the Hainan Island during 1987–2022.

Table 9. Climate and environmental indicator dynamics in the Hainan Island during 1987–2022.

Period	Total Annual Precipitation (mm)	Average Annual Minimum Temperature (Celsius)	Average Annual Maximum Temperature (Celsius)
1987	1109	17.98	24.53
1992	1415	17.27	24.03
1997	1739	17.80	24.40
2002	1689	18.62	24.73
2007	1292	17.73	24.08
2012	1917	17.52	23.76
2017	1964	18.52	24.08
2022	1590	17.73	24.77

According to the results of Pearson's correlation test (Table 10), the entire Hainan Island area and the GDP for the last year have shown a highly significant positive correlation (0.98). There is also a very significant positive correlation with the total population (0.92) and a significant negative correlation with the rural population (−0.76). From the perspective of individual counties and cities, except for Danzhou, Lingshui, and Sanya, which did not show a significant correlation between GDP and areca palm plantation area, all other counties and cities displayed significant, very significant, and highly significant positive correlations between GDP and areca palm cultivation area. The correlation coefficients ranged from a minimum of 0.83 to a maximum of 0.98. The overall correlation between the total population and areca palm plantation area in the counties and cities on Hainan Island was not pronounced. However, highly significant positive correlations were observed in Haikou, Lingshui, and Qionghai. It is worth noting that there is a negative correlation between the areca palm cultivation area and the rural population in countries and cities. The maximum negative correlations were observed in Chengmai County and Wanning City, with correlation coefficients of −0.93 and −0.92, respectively. There is a positive correlation to some extent between the areca palm cultivation area and the urban population, with

Wanning City and Chengmai County showing the most prominent correlations, with coefficients of 0.94 and 0.98, respectively.

Table 10. Pearson correlation analysis results of areca forest area with socioeconomic and climatic factors over the Hainan Island during 1987–2022.

	Total Pop	Rural Pop	Urban Pop	GDP	Precipitation	Maximum Temperature	Minimum Temperature
Hainan Island	0.92 **	−0.76 *	−0.08	0.98 ***	0.41	0.15	0.06
Baisha	−0.03	−0.03	0.15	0.87 **	0.17	0.25	0.63
Baoting	−0.18	0.09	0.48	0.92 ***	0.36	−0.02	0.62
Changjiang	0.30	−0.78 *	0.81 *	0.85 **	0.29	0.20	0.53
Chengmai	0.42	−0.93 ***	0.82 *	0.94 ***	0.18	0.37	0.67
Danzhou	0.65	−0.38	0.72 *	0.26	0.01	0.04	0.23
Ding'an	0.29	−0.80 *	−0.01	0.98 ***	0.33	0.32	0.65
Dongfang	0.48	−0.70	0.79 *	0.85 **	0.22	0.32	0.51
Haikou	0.93 ***	−0.43	0.84 **	0.88 **	0.05	0.52	0.67
Ledong	0.60	0.28	0.75 *	0.84 **	0.64	−0.22	0.52
Lingao	0.17	−0.82 *	0.53	0.86 **	0.07	0.24	0.36
Lingshui	0.90 **	0.42	0.80 *	0.58	0.76	−0.46	0.36
Qionghai	0.94 ***	−0.80 *	0.85 **	0.97 ***	0.38	0.40	0.71 *
Qiongzhong	0.01	0.25	0.44	0.83 *	0.50	0.01	0.62
Sanya	0.70	0.66	0.82	0.70	0.61	−0.45	0.55
Tunchang	0.48	−0.61	0.77 *	0.98 ***	0.38	0.27	0.65
Wanning	0.71	−0.51	0.94 ***	0.67 **	0.52	−0.21	0.51
Wenchang	0.51	−0.92 **	0.98 ***	0.92 **	0.19	0.50	0.73 *
Wuzhishan	0.36	−0.52	−0.17	0.98 ***	0.40	0.02	0.54

* $p < 0.05$, ** $p < 0.01$, *** $p < 0.001$.

4. Discussion

4.1. Historical Distribution of the Areca Palm

Throughout the areca palm mapping process, three independent survey datasets were used to map its historical distributions. High-resolution images were processed using the Res50_U-net model to map the areca palm distribution for 2022 on Hainan Island, achieving an overall accuracy of 90%. This accuracy coincides with that of Luo's machine learning-based areca palm classification method, which achieved an accuracy of 89% [58]. However, the areca palm mapping in this study was oriented to a wider range of scales. Previous research has not evaluated the spatial distribution of the areca palm on such a large scale. This study has thus demonstrated the feasibility of utilizing deep learning for large-scale areca palm classifications using high-resolution imagery. Building upon this, the study has expanded a 1 km buffer zone to generate a potential areca palm distribution area, which was used to create a historical map of the distributions on Hainan Island. Using Landsat imagery and a Random Forest algorithm with constraints on the potential distribution area, the overall accuracy for 2022 was 67%. These results indicate that the model has an adequate ability to identify areca palm distributions. Historical areca palm distribution data were also examined and found to align well with the expected growth patterns during cultivation. This study has thus successfully depicted the historical evolution of areca palm cultivation, producing, for the first time, a large-scale, high-resolution spatial distribution map over an extended period. This study has also introduced a novel approach for classifying dispersed and patchy crops. However, it should be noted that the addition of the 1 km potential distribution range will lead to some areca palms not being included in the study area, resulting in omission, which is also an aspect that needs to be improved in the future, how to obtain a more refined potential distribution of betel nut through more effective means. In addition, the accuracy of the areca palm distribution data before 2022 cannot be guaranteed due to the lack of field data classification accuracy, which means that more continuous field data will be needed in the future.

4.2. Spatiotemporal Evolution of Areca Palm Plantation on Hainan Island

From 1987 to 2022, areca palm plantations on Hainan Island exhibited a relatively clustered pattern. This clustering is influenced by both the actual cultivation practices and the limitations of the areca palm's potential distribution range. While some overestimation of clustering might occur due to these distribution range limitations, the pattern still reflects the true extent of areca palm plantations. This study identified two distinct areca palm plantation patterns on Hainan Island. The first is a high-value cluster in the southeastern region, which has shown an expansion trend over time. This pattern is most prominent in cities like Wanning and Qionghai. Wanning is renowned as the areca palm hub of China, while Qionghai has seen significant growth in areca palm cultivation in recent years, making it a key driver of local economic development. The high-value clustering enhances scale and efficiency, thus promoting the growth of the areca palm industry.

Conversely, a low-value clustering pattern is found in the southwestern and northeastern regions of Hainan Island. This pattern, particularly evident in areas like Haikou, Danzhou, and Changjiang, has not expanded. These regions do not rely heavily on the areca palm industry, which is not a major economic pillar for them. These two spatial distribution patterns highlight the significant differences in the spatial distribution and plantation practices of areca palms on Hainan Island, creating a clear east–west divide. The differences are influenced by varying levels of governmental attention, policies, and economic incentives directed toward the areca palm industry. However, the overall trend for the areca palm industry is one of rapid expansion in plantation areas, with rising prices playing a significant role in this growth. This has, however, led to rigid cultivation practices, limited the integration of technology, and fostered exploitative management. Therefore, it is necessary for the government to regulate the expansion of the areca palm industry and prevent farmers from blindly following cultivation trends. For instance, oil palm plantations in Malaysia pose a threat to peatlands, which are home to a rich diversity of flora and fauna [59]. Instead, there should be a focus on promoting the integrated application of plantation technologies to accelerate the upgrading of the areca palm industry, realize the three-dimensional comprehensive development and utilization of areca palm, and improve the output value of the unit area as well as the benefits of the vacated land for the development of the understory economy.

4.3. Mechanisms Influencing the Evolution of Areca Palm Plantation

From 1987 to 2022, the areca palm cultivation area on Hainan Island expanded dramatically, increasing from 8064 ha to 193,328 ha, over 20 times. This growth in areca palm plantations strongly correlates with Hainan Island's GDP, underscoring the crop's significant economic role. However, this correlation varies across regions. For example, Sanya shows no significant correlation, as its GDP is primarily driven by tourism rather than agriculture, and it cultivates a diverse array of crops like mangoes, coconuts, and rice alongside areca palms. Similarly, Danzhou, with rubber as its primary crop, does not show a significant correlation due to low rubber prices, despite a growing interest in switching to areca palms. In contrast, regions like Wanning and Qionghai exhibit strong correlations, reflecting the flourishing areca palm-related industries, especially in the past five years.

Field investigations revealed various areca palm cultivation types in Hainan, including plantations near farmlands, within natural tropical rainforests, in backyards, on flatlands, and in hilly and mountainous areas. The dispersed and fragmented nature of these plantations, sometimes encroaching on Hainan Tropical Rainforest National Park, raises environmental concerns, including biodiversity loss and reduced carbon sequestration capacity. Additionally, the expansion of areca palm plantations at the expense of traditional agricultural land poses risks to ecological balance, as noted in the work of **Takeuchi,** where monoculture and forest destruction can lead to ecosystem degradation and rural population outflow [60]. The areca palm trade often results in a series of associated infrastructures, including trading markets and other facilities, and these developments are frequent in urban areas. Cities and towns have developed transportation systems and

convenient trading environments. The development of the areca palm is also a microcosm of economic evolution, as the focus shifts from rural to urban areas. Indeed, the areca palm is a high-value cash crop that can be lucrative for farmers; however, achieving large-scale planting and efficient management while ensuring ecological sustainability and a harmonious relationship between humans and nature are significant challenges for Hainan Island and the rest of the world. Srinivasan's work provides an example of India's oil palm. However, the current expansion of oil palm cultivation in India comes at the cost of biodiversity-rich landscapes. But their model suggests that, on a national scale, India seems to have viable options to meet its projected palm oil demand without compromising its biodiversity or food security [61]. Can the planting of Areca palm in Hainan meet the needs of the forest through macro policy regulation and control under the consideration of the existing planting concentration? On a more precise spatial scale, areca palm cultivation needs to take into account local climatic conditions, biodiversity, local agricultural input ratios, and trade-offs between economy and social security. China's policy decisions on areca palm have largely mitigated the current set of problems facing China's tropical rainforests.

5. Conclusions

This study represents a significant advancement in understanding the spatial distribution and driving forces behind areca palm cultivation on Hainan Island, China, by leveraging the power of satellite remote sensing and deep learning. By producing the first large-scale, long-term spatial distribution analysis at a 30 m resolution, the research has not only achieved high classification accuracy but also provided critical insights into the socioeconomic and environmental factors influencing areca palm expansion. The spatiotemporal dynamics revealed in this study underscore the complex interplay between agricultural practices and broader regional development trends. Importantly, the identification of two distinct areca palm plantation patterns offers a new lens through which to assess the sustainability of current practices. These findings highlight the need for future research to delve deeper into the long-term ecological impacts of these plantation patterns and to refine remote sensing methodologies to further enhance accuracy and resolution. Furthermore, this research underscores the broader implications for sustainable agricultural policy, not only in China but also in other regions facing similar challenges. By scaling the models and incorporating more recent advancements in remote sensing and machine learning, future studies could expand this work to additional countries and regions, providing valuable data to support global agricultural sustainability efforts. Ultimately, this research serves as a crucial reference point for developing policies that promote sustainable agricultural practices, contributing to the global discourse on agricultural and environmental resilience.

Author Contributions: Z.Q.: Conceptualization, methodology, formal analysis, resources, and project administration. H.P.: Methodology, formal analysis, and writing—review and editing. C.W.: Methodology, writing—original draft, software, validation, and writing—review and editing. Z.Y.: Software, formal analysis, and visualization. R.L.: Software and visualization. C.F.: Visualization. Y.W.: Data curation. J.Q.: Data curation. Y.X.: Project administration. Z.L.: Formal analysis. All authors have read and agreed to the published version of the manuscript.

Data Availability Statement: These data can be found here: https://figshare.com/articles/dataset/Hainan_Historical_Areca_distribution_from_1987_to_2022/24452773 (accessed on 19 September 2024).

Conflicts of Interest: The authors declare no conflicts of interest.

References

1. Delpeuch, C.; Leblois, A. The Elusive Quest for Supply Response to Cash-Crop Market Reforms in Sub-Saharan Africa: The Case of Cotton. *World Dev.* **2014**, *64*, 521–537. [CrossRef]
2. Su, S.; Wan, C.; Li, J.; Jin, X.; Pi, J.; Zhang, Q.; Weng, M. Economic benefit and ecological cost of enlarging tea cultivation in subtropical China: Characterizing the trade-off for policy implications. *Land Use Policy* **2017**, *66*, 183–195. [CrossRef]
3. Herrmann, R.; Jumbe, C.; Bruentrup, M.; Osabuohien, E. Competition between biofuel feedstock and food production: Empirical evidence from sugarcane outgrower settings in Malawi. *Biomass Bioenergy* **2018**, *114*, 100–111. [CrossRef]
4. Wiréhn, L. Nordic agriculture under climate change: A systematic review of challenges, opportunities and adaptation strategies for crop production. *Land Use Policy* **2018**, *77*, 63–74. [CrossRef]
5. Li, J.; Zhang, Z.; Jin, X.; Chen, J.; Zhang, S.; He, Z.; Li, S.; He, Z.; Zhang, H.; Xiao, H. Exploring the socioeconomic and ecological consequences of cash crop cultivation for policy implications. *Land Use Policy* **2018**, *76*, 46–57. [CrossRef]
6. Talhelm, T. Emerging evidence of cultural differences linked to rice versus wheat agriculture. *Curr. Opin. Psychol.* **2020**, *32*, 81–88. [CrossRef]
7. Buente, W.; Dalisay, F.; Pokhrel, P.; Kramer, H.K.; Pagano, I. An Instagram-Based Study to Understand Betel Nut Use Culture in Micronesia: Exploratory Content Analysis. *J. Med. Internet Res.* **2020**, *22*, e13954. [CrossRef]
8. Elbakidze, M.; Surová, D.; Muñoz-Rojas, J.; Persson, J.-O.; Dawson, L.; Plieninger, T.; Pinto-Correia, T. Perceived benefits from agroforestry landscapes across North-Eastern Europe: What matters and for whom? *Landsc. Urban Plan.* **2021**, *209*, 104044. [CrossRef]
9. Liu, P.; Li, W.; Yu, Y.; Tang, R.; Guo, X.; Wang, B.; Yang, B.; Zhang, L. How much will cash forest encroachment in rainforests cost? A case from valuation to payment for ecosystem services in China. *Ecosyst. Serv.* **2019**, *38*, 100949. [CrossRef]
10. Qaim, M.; Sibhatu, K.T.; Siregar, H.; Grass, I. Environmental, Economic, and Social Consequences of the Oil Palm Boom. *Annu. Rev. Resour. Econ.* **2020**, *12*, 321–344. [CrossRef]
11. Ansari, A.; Mahmood, T.; Bagga, P.; Ahsan, F.; Shamim, A.; Ahmad, S.; Shariq, M.; Parveen, S. *Areca catechu*: A phytopharmacological legwork. *Food Front.* **2021**, *2*, 163–183. [CrossRef]
12. Zhang, H.; Wei, Y.; Shi, H. First Report of Anthracnose Caused by *Colletotrichum kahawae* subsp. *ciggaro* on Areca in China. *Plant Dis.* **2020**, *104*, 1871. [CrossRef]
13. Li, J.; Jia, X.; Liu, L.; Cao, X.; Xiong, Y.; Yang, Y.; Zhou, H.; Yi, M.; Li, M. Comparative biochemical and transcriptome analysis provides insights into the regulatory mechanism of striped leaf albinism in arecanut (*Areca catechu* L.). *Ind. Crops Prod.* **2020**, *154*, 112734. [CrossRef]
14. Myers, A.L. Metabolism of the areca alkaloids—Toxic and psychoactive constituents of the areca (betel) nut. *Drug Metab. Rev.* **2022**, *54*, 343–360. [CrossRef]
15. Moss, W.J. The Seeds of Ignorance—Consequences of a Booming Betel-Nut Economy. *N. Engl. J. Med.* **2022**, *387*, 1059–1061. [CrossRef]
16. Su, S.-Y.; Chen, W.-T.; Chiang, C.-J.; Yang, Y.-W.; Lee, W.-C. Oral cancer incidence rates from 1997 to 2016 among men in Taiwan: Association between birth cohort trends and betel nut consumption. *Oral Oncol.* **2020**, *107*, 104798. [CrossRef]
17. Mehrtash, H.; Duncan, K.; Parascandola, M.; David, A.; Gritz, E.R.; Gupta, P.C.; Mehrotra, R.; Amer Nordin, A.S.; Pearlman, P.C.; Warnakulasuriya, S.; et al. Defining a global research and policy agenda for betel quid and areca nut. *Lancet Oncol.* **2017**, *18*, e767–e775. [CrossRef]
18. Warnakulasuriya, S.; Chen, T.H.H. Areca Nut and Oral Cancer: Evidence from Studies Conducted in Humans. *J. Dent. Res.* **2022**, *101*, 1139–1146. [CrossRef]
19. Lechner, M.; Breeze, C.E.; Vaz, F.; Lund, V.J.; Kotecha, B. Betel nut chewing in high-income countries—Lack of awareness and regulation. *Lancet Oncol.* **2019**, *20*, 181–183. [CrossRef]
20. Murphy, K.L.; Liu, M.; Herzog, T.A. Confirmatory factor analysis and structural equation modeling of socio-cultural constructs among chamorro and non-chamorro micronesian betel nut chewers. *Ethn. Health* **2019**, *24*, 724–735. [CrossRef]
21. Yang, B.; Chen, H.; Chen, W.; Chen, W.; Zhong, Q.; Zhang, M.; Pei, J. Edible Quality Analysis of Different Areca Nuts: Compositions, Texture Characteristics and Flavor Release Behaviors. *Foods* **2023**, *12*, 1749. [CrossRef] [PubMed]
22. Zhou, B.; Zhu, W.; Ren, C. First steps to regulate advertising of areca nut in China. *Lancet Oncol.* **2019**, *20*, 615–616. [CrossRef] [PubMed]
23. Chaves, M.E.D.; Picoli, M.C.A.; Sanches, I.D. Recent Applications of Landsat 8/OLI and Sentinel-2/MSI for Land Use and Land Cover Mapping: A Systematic Review. *Remote Sens.* **2020**, *12*, 3062. [CrossRef]
24. Gao, F.; Zhang, X. Mapping Crop Phenology in Near Real-Time Using Satellite Remote Sensing: Challenges and Opportunities. *J. Remote Sens.* **2021**, *2021*, 8379391. [CrossRef]
25. Mahlayeye, M.; Darvishzadeh, R.; Nelson, A. Cropping Patterns of Annual Crops: A Remote Sensing Review. *Remote Sens.* **2022**, *14*, 2404. [CrossRef]
26. Freudenberg, M.; Nölke, N.; Agostini, A.; Urban, K.; Wörgötter, F.; Kleinn, C. Large Scale Palm Tree Detection in High Resolution Satellite Images Using U-Net. *Remote Sens.* **2019**, *11*, 312. [CrossRef]
27. Li, W.; Fu, H.; Yu, L.; Cracknell, A. Deep Learning Based Oil Palm Tree Detection and Counting for High-Resolution Remote Sensing Images. *Remote Sens.* **2017**, *9*, 22. [CrossRef]

28. Cheng, Y.; Yu, L.; Xu, Y.; Lu, H.; Cracknell, A.P.; Kanniah, K.; Gong, P. Mapping oil palm extent in Malaysia using ALOS-2 PALSAR-2 data. *Int. J. Remote Sens.* **2018**, *39*, 432–452. [CrossRef]

29. Lee, J.S.H.; Wich, S.; Widayati, A.; Koh, L.P. Detecting industrial oil palm plantations on Landsat images with Google Earth Engine. *Remote Sens. Appl. Soc. Environ.* **2016**, *4*, 219–224. [CrossRef]

30. Li, H.; Song, X.-P.; Hansen, M.C.; Becker-Reshef, I.; Adusei, B.; Pickering, J.; Wang, L.; Wang, L.; Lin, Z.; Zalles, V.; et al. Development of a 10-m resolution maize and soybean map over China: Matching satellite-based crop classification with sample-based area estimation. *Remote Sens. Environ.* **2023**, *294*, 113623. [CrossRef]

31. Johnson, D.M. Using the Landsat archive to map crop cover history across the United States. *Remote Sens. Environ.* **2019**, *232*, 111286. [CrossRef]

32. Carrasco, L.; Fujita, G.; Kito, K.; Miyashita, T. Historical mapping of rice fields in Japan using phenology and temporally aggregated Landsat images in Google Earth Engine. *ISPRS J. Photogramm. Remote Sens.* **2022**, *191*, 277–289. [CrossRef]

33. Wulder, M.A.; Roy, D.P.; Radeloff, V.C.; Loveland, T.R.; Anderson, M.C.; Johnson, D.M.; Healey, S.; Zhu, Z.; Scambos, T.A.; Pahlevan, N.; et al. Fifty years of Landsat science and impacts. *Remote Sens. Environ.* **2022**, *280*, 113195. [CrossRef]

34. Asgarian, A.; Soffianian, A.; Pourmanafi, S. Crop type mapping in a highly fragmented and heterogeneous agricultural landscape: A case of central Iran using multi-temporal Landsat 8 imagery. *Comput. Electron. Agric.* **2016**, *127*, 531–540. [CrossRef]

35. Jin, Y.; Guo, J.; Ye, H.; Zhao, J.; Huang, W.; Cui, B. Extraction of Arecanut Planting Distribution Based on the Feature Space Optimization of PlanetScope Imagery. *Agriculture* **2021**, *11*, 371. [CrossRef]

36. Gumma, M.K.; Nelson, A.; Thenkabail, P.S.; Singh, A.N. Mapping rice areas of South Asia using MODIS multitemporal data. *J. Appl. Remote Sens.* **2011**, *5*, 053547. [CrossRef]

37. Jia, M.; Wang, Z.; Mao, D.; Ren, C.; Song, K.; Zhao, C.; Wang, C.; Xiao, X.; Wang, Y. Mapping global distribution of mangrove forests at 10-m resolution. *Sci. Bull.* **2023**, *68*, 1306–1316. [CrossRef]

38. Fluet-Chouinard, E.; Stocker, B.D.; Zhang, Z.; Malhotra, A.; Melton, J.R.; Poulter, B.; Kaplan, J.O.; Goldewijk, K.K.; Siebert, S.; Minayeva, T.; et al. Extensive global wetland loss over the past three centuries. *Nature* **2023**, *614*, 281–286. [CrossRef]

39. Georganos, S.; Grippa, T.; Vanhuysse, S.; Lennert, M.; Shimoni, M.; Kalogirou, S.; Wolff, E. Less is more: Optimizing classification performance through feature selection in a very-high-resolution remote sensing object-based urban application. *GIScience Remote Sens.* **2018**, *55*, 221–242. [CrossRef]

40. Li, Y.; Zhang, H.; Xue, X.; Jiang, Y.; Shen, Q. Deep learning for remote sensing image classification: A survey. *WIREs Data Min. Knowl. Discov.* **2018**, *8*, e1264. [CrossRef]

41. Cheng, G.; Xie, X.; Han, J.; Guo, L.; Xia, G.-S. Remote Sensing Image Scene Classification Meets Deep Learning: Challenges, Methods, Benchmarks, and Opportunities. *IEEE J. Sel. Top. Appl. Earth Obs. Remote Sens.* **2020**, *13*, 3735–3756. [CrossRef]

42. Lin, Y.-z.; Nie, Z.-h.; Ma, H.-w. Structural Damage Detection with Automatic Feature-Extraction through Deep Learning: Structural damage detection with automatic feature-extraction through deep learning. *Comput.-Aided Civ. Infrastruct. Eng.* **2017**, *32*, 1025–1046. [CrossRef]

43. Janiesch, C.; Zschech, P.; Heinrich, K. Machine learning and deep learning. *Electron. Mark.* **2021**, *31*, 685–695. [CrossRef]

44. Shinde, P.P.; Shah, S. A Review of Machine Learning and Deep Learning Applications. In Proceedings of the 2018 Fourth International Conference on Computing Communication Control and Automation (ICCUBEA), Pune, India, 6–18 August 2018; pp. 1–6.

45. Liang, J.; Gong, J.; Li, W. Applications and impacts of Google Earth: A decadal review (2006–2016). *ISPRS J. Photogramm. Remote Sens.* **2018**, *146*, 91–107. [CrossRef]

46. Schmidt, G.; Jenkerson, C.B.; Masek, J.; Vermote, E.; Gao, F. *Landsat Ecosystem Disturbance Adaptive Processing System (LEDAPS) Algorithm Description*; 2013–1057; USGS: Reston, VA, USA, 2013; p. 27.

47. Vermote, E.; Roger, J.C.; Franch, B.; Skakun, S. LaSRC (Land Surface Reflectance Code): Overview, application and validation using MODIS, VIIRS, LANDSAT and Sentinel 2 data's. In Proceedings of the IGARSS 2018—2018 IEEE International Geoscience and Remote Sensing Symposium, Valencia, Spain, 22–27 July 2018; pp. 8173–8176.

48. Brown, C.F.; Brumby, S.P.; Guzder-Williams, B.; Birch, T.; Hyde, S.B.; Mazzariello, J.; Czerwinski, W.; Pasquarella, V.J.; Haertel, R.; Ilyushchenko, S.; et al. Dynamic World, Near real-time global 10 m land use land cover mapping. *Sci. Data* **2022**, *9*, 251. [CrossRef]

49. He, K.; Zhang, X.; Ren, S.; Sun, J. Deep Residual Learning for Image Recognition. In Proceedings of the IEEE Conference on Computer Vision and Pattern Recognition (CVPR), Las Vegas, NV, USA, 27–30 June 2016. [CrossRef]

50. Ronneberger, O.; Fischer, P.; Brox, T. U-Net: Convolutional Networks for Biomedical Image Segmentation. In *Medical Image Computing and Computer-Assisted Intervention—MICCAI 2015*; Navab, N., Hornegger, J., Wells, W.M., Frangi, A.F., Eds.; Springer International Publishing: Cham, Switzerland, 2015; Volume 9351, pp. 234–241.

51. Li, D.; Lin, B.; Wang, X.; Guo, Z. High-Performance Polarization Remote Sensing with the Modified U-Net Based Deep-Learning Network. *IEEE Trans. Geosci. Remote Sens.* **2022**, *60*, 1–10. [CrossRef]

52. Shamsolmoali, P.; Zareapoor, M.; Wang, R.; Zhou, H.; Yang, J. A Novel Deep Structure U-Net for Sea-Land Segmentation in Remote Sensing Images. *IEEE J. Sel. Top. Appl. Earth Obs. Remote Sens.* **2019**, *12*, 3219–3232. [CrossRef]

53. Fan, X.; Yan, C.; Fan, J.; Wang, N. Improved U-Net Remote Sensing Classification Algorithm Fusing Attention and Multiscale Features. *Remote Sens.* **2022**, *14*, 3591. [CrossRef]

54. Ayushi; Buttar, P.K. Satellite Imagery Analysis for Crop Type Segmentation Using U-Net Architecture. *Procedia Comput. Sci.* **2024**, *235*, 3418–3427. [CrossRef]

55. Kingma, D.P.; Ba, J. Adam: A method for stochastic optimization. *arXiv* **2014**, arXiv:1412.6980.
56. Breiman, L. Random Forests. *Mach. Learn.* **2001**, *45*, 5–32. [CrossRef]
57. Lee, J.; Li, S. Extending Moran's Index for Measuring Spatiotemporal Clustering of Geographic Events. *Geogr. Anal.* **2017**, *49*, 36–57. [CrossRef]
58. Luo, H.; Li, M.; Dai, S.; Li, H.; Li, Y.; Hu, Y.; Zheng, Q.; Yu, X.; Fang, J. Combinations of Feature Selection and Machine Learning Algorithms for Object-Oriented Betel Palms and Mango Plantations Classification Based on Gaofen-2 Imagery. *Remote Sens.* **2022**, *14*, 1757. [CrossRef]
59. Mayes, S. The History and Economic Importance of the Oil Palm. In *The Oil Palm Genome*; Ithnin, M., Kushairi, A., Eds.; Springer International Publishing: Cham, Switzerland, 2020; pp. 1–8.
60. Takeuchi, K.; Ichikawa, K.; Elmqvist, T. Satoyama landscape as social–ecological system: Historical changes and future perspective. *Curr. Opin. Environ. Sustain.* **2016**, *19*, 30–39. [CrossRef]
61. Srinivasan, U.; Velho, N.; Lee, J.S.H.; Chiarelli, D.D.; Davis, K.F.; Wilcove, D.S. Oil palm cultivation can be expanded while sparing biodiversity in India. *Nat. Food* **2021**, *2*, 442–447. [CrossRef]